

光学学报

太赫兹多维复用与折射率传感集成器件

揭璐, 李海粟*, 刘亚静, 王建帅, 任国斌, 裴丽

北京交通大学光波技术研究所全光网络与现代通信网教育部重点实验室, 北京 100044

摘要 提出了一种基于亚波长偏振保持光纤的多维复用与折射率(RI)传感集成器件。该器件由定向耦合器、Y型分束器和布拉格光栅器件构成,能够同时实现三维空间中偏振和频率(解)复用、色散补偿以及RI传感功能。集成器件下行端口输出偏振解复用后的 x 偏振态,其在0.25 THz频率处的传输率和消光比分别为-5.94 dB和15.16 dB。此后,原波导中 y 偏振态(工作频率为0.25 THz)与 x 偏振态(工作频率为0.27 THz)复用后于直通端口输出,传输率分别为-7.20 dB和-2.02 dB。同时,集成的均匀光栅和 π 相移光栅可分别实现色散补偿(群速度色散为 $-109.4 \text{ ps} \cdot \text{THz}^{-1} \cdot \text{mm}^{-1}$)和RI传感(灵敏度为0.181 THz/RIU)功能。基于太赫兹亚波长光纤的集成器件在下一代通感一体化信息系统中具有良好的应用前景。

关键词 光学器件; 太赫兹; 耦合器; 复用器; 传感器

中图分类号 O436 文献标志码 A

DOI: 10.3788/AOS231686

1 引言

为满足数据传输容量激增的需求,下一代无线通信系统的载波频率将不可避免地向具有超大带宽的太赫兹频段(0.1~10.0 THz)转移^[1-5]。得益于高质量太赫兹信号源^[6]和探测器^[7]的发展,各种太赫兹无线和有线通信系统迅速涌现。最近,美国东北大学利用肖特基二极管技术在2.03 km距离内实现了2 Gbit/s的太赫兹无线通信^[8]。同时,南洋理工大学展示了工作频率为340 GHz时基于硅拓扑光子波导的单通道160 Gbit/s通信链路^[9]。无论是在无线还是有线通信系统中,提供信号处理和集成功能的太赫兹器件都至关重要^[10-13]。

根据波导结构,太赫兹波导器件可分为光纤器件和硅基平面器件。对于长度一般为几厘米的片上互连来说,平面器件是非常理想的选择^[14-16]。例如,华中科技大学提出了一种太赫兹硅基多维(解)复用器,该复用器由环形谐振器和偏振分束器-旋转器组成,可同时操纵偏振和频率,他们通过实验实现了0.38 THz频率处8 Gbit/s的数据传输速率^[17]。然而,平面器件是在高电阻率晶圆上制成的,仅能够在二维(2D)平面集成,这限制了器件的空间自由度。对于长达数米的太赫兹通信链路来说,光纤器件是实现信号传输和“在线”操控(即在太赫兹波沿光纤器件传输的过程中进行操控)的关键技术^[1,18]。基于太赫兹光纤的耦合

器^[19-20]、分束器^[11,21]、色散补偿器^[22]和滤波器^[10,23]等可提供(解)复用、路由、多种信号传感功能。台湾大学提出了一种由两根方管形光纤组成的太赫兹漏模定向耦合器,由于中空结构之间的弱模式耦合,该耦合器需要10.8 cm的耦合长度^[19]。蒙特利尔大学提出了一种基于光栅耦合器的频分复用器,能够对比特率高达6 Gbit/s的太赫兹信号进行(解)复用^[24]。马尔堡大学利用3D打印机制造出了弯曲半径小于10 mm的Y型分束器,其额外的弯曲损耗可以忽略不计^[21]。蒙特利尔大学还展示了一种基于金属空芯波导的色散补偿器,其在0.14 THz附近的负群速度色散(GVD)约为 $-25 \text{ ps} \cdot \text{THz}^{-1} \cdot \text{mm}^{-1}$ ^[22]。北京交通大学设计并制作了基于太赫兹亚波长矩形聚合物光纤的光栅,该光栅可同时对两种偏振态进行滤波,并且阻带的消光比(ER)超过20.9 dB,半峰全宽(FWHM)约为21.1 GHz^[10]。此外,北京交通大学提出了一种基于圆对称亚波长光纤的相移光栅,探索了其在折射率(RI)传感方面的潜力^[25]。

然而,大多数已报道的太赫兹光纤器件只提供单一功能。对于丰富的太赫兹波应用领域,集成多种功能的光纤器件仍有很大的发展空间。本文提出了一种基于太赫兹亚波长光纤的多维复用与RI传感集成器件。该器件由两个定向耦合器、一个50/50 Y型分束器、一个均匀布拉格光栅和一个 π 相移布拉格光栅组成,可实现偏振-频率(解)复用、色散补偿以及环境RI

收稿日期: 2023-10-23; 修回日期: 2023-11-30; 录用日期: 2023-12-13; 网络首发日期: 2023-12-23

基金项目: 中央高校基本科研业务费专项资金(2022JBZY004)、国家自然科学基金(62075007, 62275011)

通信作者: *lihaisu@bjtu.edu.cn

传感功能。本文工作突破了硅基波导器件仅能在2D空间进行集成的限制,丰富了太赫兹波导器件在信息传输、处理等方面的应用。

2 集成器件结构及设计方法

本文提出的多维复用与RI传感集成器件结构如图1(a)所示,该器件由定向耦合器、色散补偿器、Y型分束器和相移光栅传感器组成。从输入端口(in port)进

发射中心频率为0.25 THz且带宽为10 GHz的两种正交偏振模式。然后,0.25 THz的x偏振信号通过定向耦合器耦合到下行端口(drop port),再通过均匀光栅进行色散补偿,而0.25 THz的y偏振信号通过Y型分束器分成两路信号。其中一路信号与来自添加端口(add port)的中心频率为0.27 THz的x偏振信号进行频率复用,另一路信号则通过 π 相移光栅进行环境RI传感。

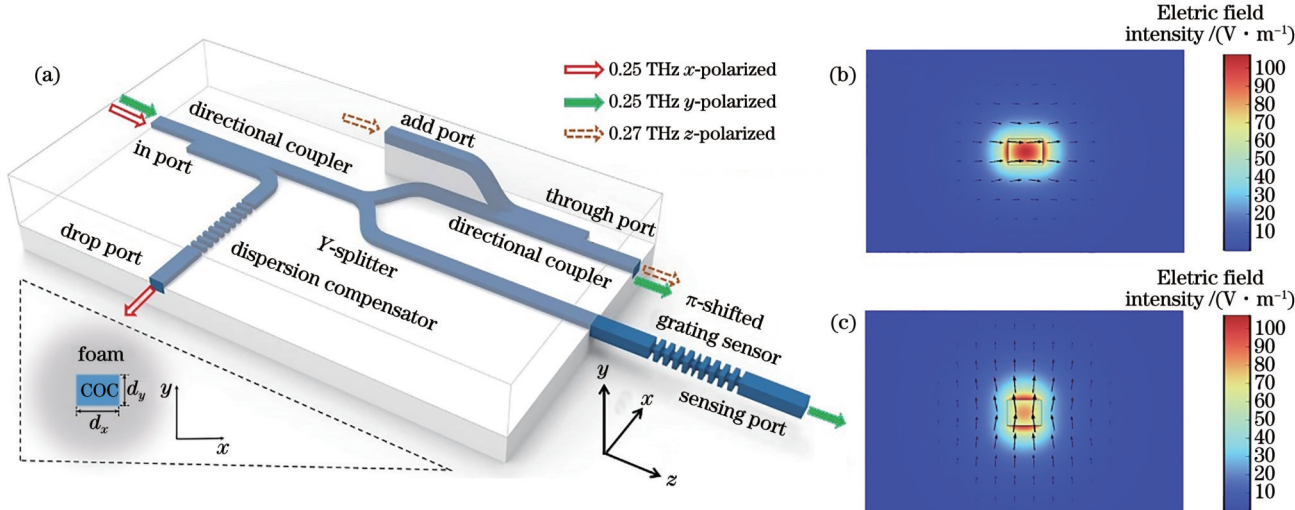


图1 太赫兹多维复用与RI传感集成器件模型图及亚波长光纤传输性能仿真结果。(a)器件的3D结构;光纤中(b)x偏振态及(c)y偏振态在0.25 THz时芯子周围的归一化电场分布(箭头代表电矢量)

Fig. 1 Schematic diagram of multidimensional-multiplexing and RI sensing integrated device, and simulation results of subwavelength fiber transmission performance. (a) 3D structure of device; normalized electric field intensity of (b) x -polarized modes and (c) y -polarized modes for fiber at 0.25 THz (arrows represent electric vectors)

如图1(a)的左下方插图所示,本文提出的器件均基于亚波长聚合物光纤。通过将光纤横截面设计为矩形来引入结构各向异性,从而实现高双折射(在0.24~0.28 THz频带范围内,双折射高于0.03)的偏振保持传输,如图2(a)所示。由于环烯烃共聚物(COC)材料(TOPAS 5013L-10)在太赫兹范围内具有较低的吸收损耗^[26-27],因此选择它作为亚波长光纤的主材料。使用太赫兹时域光谱系统(THz-TDS)测量了COC在0.24~0.28 THz范围内的光学特性,其吸收系数小于0.02 mm\$^{-1}\$,RI几乎是一个常数(1.5365)^[28]。基于微机械加工技术,采用COC材料制作了太赫兹亚波长矩形芯光纤^[29]。制备并通过实验测量了基于上述光纤的均匀光栅,在0.15 THz工作频率处,x偏振信号可获得高达\$-188 \text{ ps}\cdot\text{THz}^{-1}\cdot\text{mm}^{-1}\$的色散补偿^[28]。此外,为了防止器件受到外部环境的干扰,将其封装在泡沫包层中^[30]。实验结果表明,在0.24~0.28 THz频率范围内,泡沫的RI为1.004,吸收系数小于0.003 mm\$^{-1}\$^[28]。选取的泡沫材料参数与空气接近,这可以有效降低泡沫包层对模式传输的影响。本文使用基于有限元法的商业软件COMSOL Multiphysics^[31]对亚波长光纤横截面进行设计。根据之前的测量结果,在仿真中应用

频率依赖的复折射率对COC和泡沫材料进行定义^[28]。仿真中加入完美匹配层(PML),用于模拟无限大的泡沫包层,其中PML与器件边缘的距离超过15个波长以模拟足够大的区域。通过仿真发现,截面参数为\$d_x=0.600 \text{ mm}\$和\$d_y=0.445 \text{ mm}\$的亚波长光纤在0.24~0.28 THz频带范围内可实现低损耗(低于\$0.051 \text{ dB}\cdot\text{mm}^{-1}\$)、高双折射(高于0.03)传输。从图1(b)和图1(c)可以看出,该光纤支持两种正交模式的稳定传输(偏振方向沿x轴和y轴的模式即x偏振态和y偏振态)。通过将光纤截面设计成矩形来引入双折射,从而实现简并分离,使得x偏振态和y偏振态的传输性能有着较大差异。如图2(b)所示,0.25 THz的x偏振态和y偏振态的功率束缚因子\$\eta\$分别为0.56和0.47。此外,通过仿真对比了两种正交模式在有无泡沫包层的光纤中的传输损耗和群速度色散。如图2(c)所示,添加泡沫包层后的损耗增加了约\$0.05 \text{ dB}\cdot\text{mm}^{-1}\$,这是因为泡沫对太赫兹波的吸收略大于空气。不过,如图2(d)所示,泡沫包层对群速度色散的影响却很小,这是因为泡沫的RI与空气的RI非常接近。接下来,使用时域有限差分法(FDTD)对亚波长光纤集成器件进行设计,其中亚波

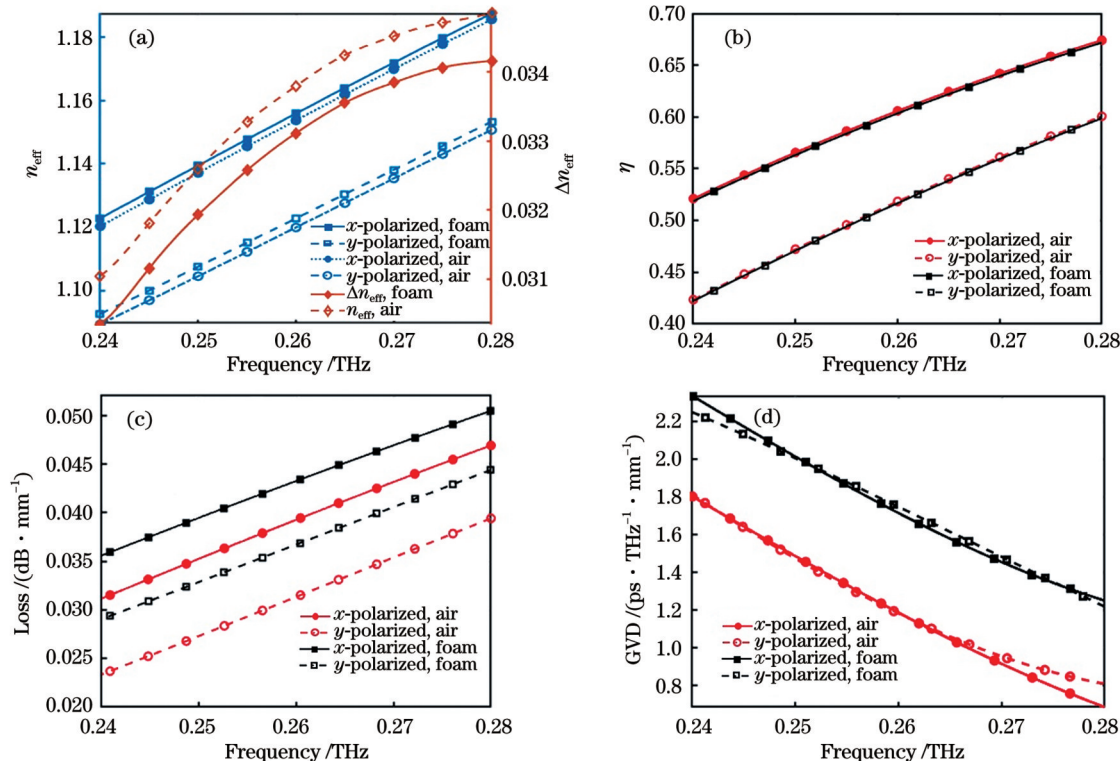


图2 亚波长光纤传输性能仿真结果。有无泡沫包层时光纤中 x 偏振态和 y 偏振态的(a)芯子中的有效折射率和双折射率、(b)功率束缚因子、(c)损耗以及(d)群速度色散(GVD)随频率的变化曲线

Fig. 2 Simulation results of subwavelength fiber transmission performance. (a) Effective RI and birefringence, (b) fractional power in core, (c) loss, and (d) GVD values of x -polarized and y -polarized states with and without foam cladding for fiber as functions of frequency

长光纤的参数和边界条件与 COMSOL 仿真保持一致。此外,太赫兹脉冲使用 x 或 y 偏振光纤模式发射,而且在器件的输出端口放置了场强监视器用于测量透射率。

3 器件仿真及结果分析

3.1 弯曲光纤

弯曲光纤对于信号的路由以及耦合至关重要。在上述亚波长光纤的基础上,本文根据贝塞尔曲线提出了两种弯曲光纤:90°弯曲光纤和S型弯曲光纤。这两种光纤又可以分别设计成沿 x 轴或 y 轴弯曲的光纤,从而形成图3所示的4种结构。将沿 x 轴弯曲的光纤定义为 x 轴弯曲光纤,如图3(a)、(b)所示(x 轴表示光纤的弯曲方向)。同样,图3(c)、(d)分别展示了 y 轴90°弯曲和S型弯曲光纤(y 轴表示光纤的弯曲方向)。此外,由于贝塞尔曲线的弯曲半径不是常数,因此使用曲率半径的最小值代表弯曲半径。接下来对具有不同弯曲半径的光纤的传输性能进行分析。

图4(a)、(b)分别为弯曲半径为2~10 mm的90°和S型弯曲光纤在0.25 THz时的传输情况。传输率随弯曲半径的增加而增大,而当弯曲半径大于7 mm时,两种弯曲光纤中 x 偏振态的传输率趋于平坦。此外, y 偏振态的传输率低于 x 偏振态,这是因为芯子对 y

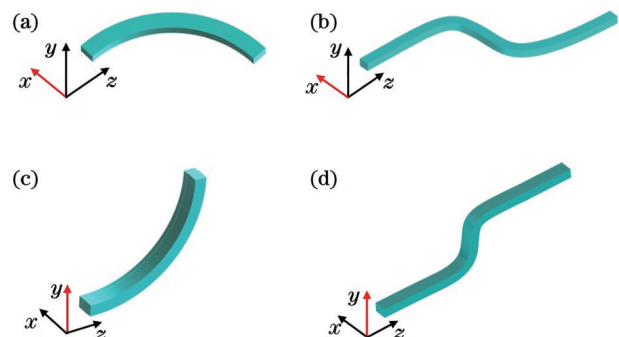


图3 4种弯曲光纤的结构示意图。(a) x 轴90°弯曲光纤;(b) x 轴S型弯曲光纤;(c) y 轴90°弯曲光纤;(d) y 轴S型弯曲光纤

Fig. 3 Schematics of four types of bent fibers. (a) x -bent 90° fiber; (b) x -bent S-shaped fiber; (c) y -bent 90° fiber; (d) y -bent S-shaped fiber

偏振态的束缚能力较弱,弯曲导致了更多的功率泄漏。图4(c)、(d)分别为弯曲半径为10 mm的90°和S型弯曲光纤在0.24~0.28 THz频率范围内的传输曲线。由于功率泄漏和材料吸收的共同作用,弯曲光纤的传输率随着频率的增加先提高后降低。此外,从图4中可以看出,在0.24~0.28 THz频率范围内,弯曲半径为10 mm的S型弯曲光纤的传输率略高于90°弯曲光纤,这是因为S型弯曲光纤的弯曲路径更加平滑。

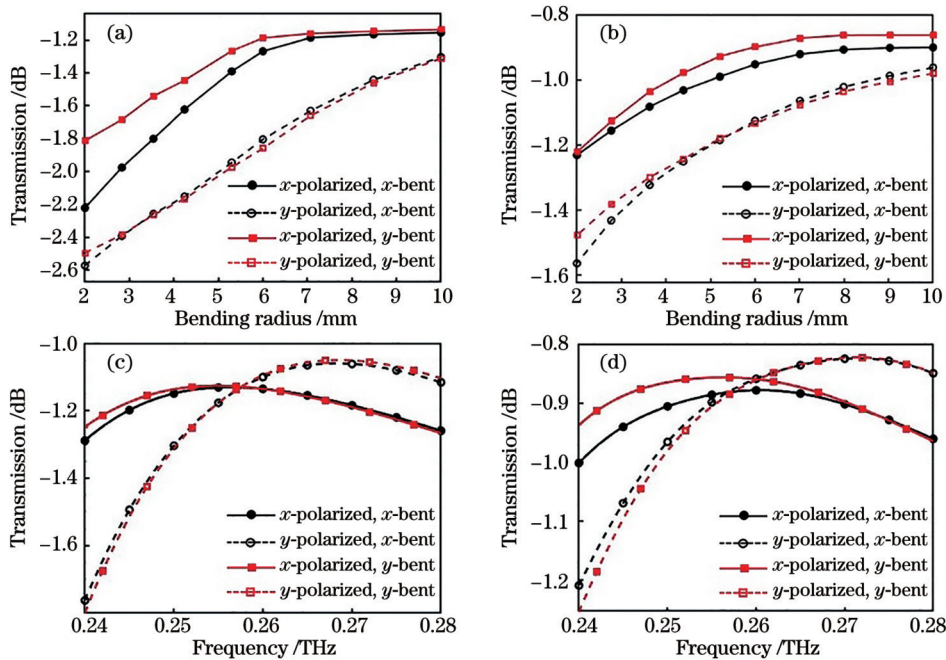


图 4 90°和 S 型弯曲光纤的传输率随弯曲半径以及频率的变化。(a)90°弯曲光纤和(b)S型弯曲光纤在 0.25 THz 频率处的传输率随弯曲半径的变化;(c)弯曲半径为 10 mm 的 90°弯曲光纤和(d)S型弯曲光纤的传输率随频率的变化

Fig. 4 Transmission varying with bend radius and frequency for 90° and S-shaped bending fibers. Transmission of (a) 90° and (b) S-shaped bending fibers at 0.25 THz as a function of bending radius; transmission of (c) 90° and (d) S-shaped bending fibers with bending radius of 10 mm as a function of frequency

Y型分束器可使用两个弯曲半径均为 10 mm 的 S 型光纤组合而成,其结构如图 5(a)所示(x 轴表示光纤

的弯曲方向)。仿真结果显示,该 Y型分束器可以平均分配 x 偏振态和 y 偏振态,功率分布和传输率分别

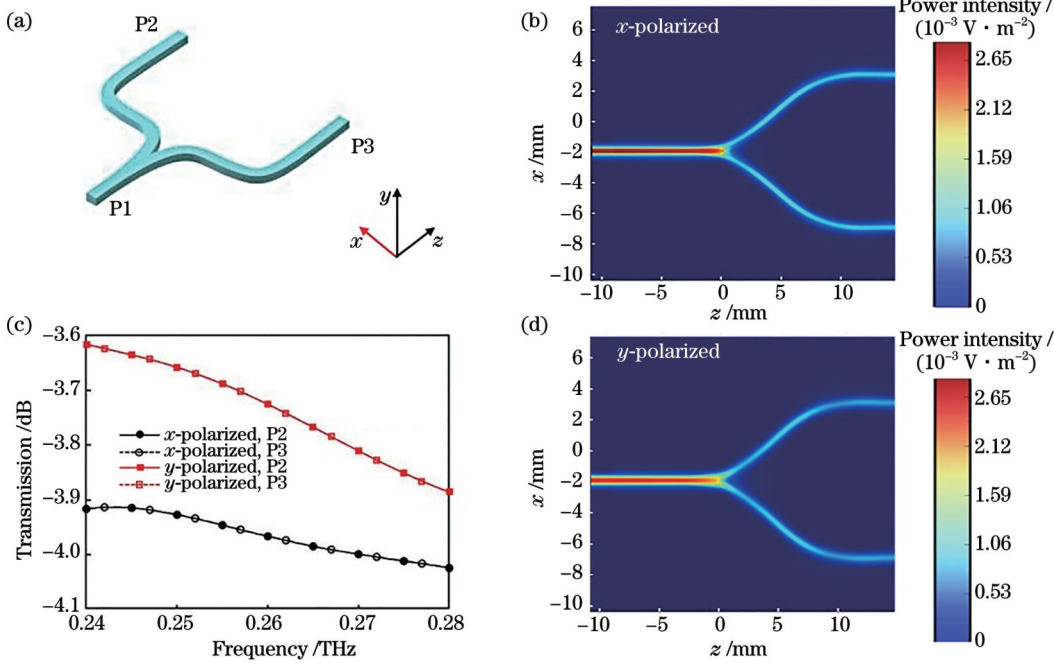


图 5 Y型分束器结构图及分束性能仿真结果。(a)50/50 Y型分束器示意图,其中输入端口为 P1,两个输出端口为 P2 和 P3;(b)Y型分束器中 x 偏振态在 0.25 THz 频率处的功率分布;(c)从 Y型分束器的两个输出端口 P2 和 P3 输出模式的传输率随频率的变化曲线;(d)Y型分束器中 y 偏振态在 0.25 THz 频率处的功率分布

Fig. 5 Structure diagram of Y-splitter and simulation results of beam splitting performance. (a) Schematic of 50/50 Y-splitter. Input port is P1, while two outputs are P2 and P3; (b) simulated power distribution of x-polarized state for the Y-splitter at 0.25 THz; (c) transmission of Y-splitter at P2 and P3 ports as a function of frequency; (d) simulated power distribution of y-polarized state for Y-splitter at 0.25 THz

如图5(b)、(c)、(d)所示。此外,从图5(c)中可以明显看出x偏振态的传输率低于y偏振态,这是因为光纤对x偏振态有着更强的模式约束,导致材料吸收损耗比y偏振态更为显著[图2(c)]。

3.2 定向耦合器

定向耦合器是设计频率和偏振(解)复用系统的关键部件,可用于同时处理频率和偏振信息。图6(a)是

由两根紧贴在一起的亚波长光纤组成的定向耦合器,光纤间的耦合长度可根据超模理论和相位匹配原理进行设计^[32-34]。然而,为了实现两根亚波长光纤之间的有效耦合(耦合长度为固定值),只有其中一种偏振态沿直光纤耦合出来,由于光纤的不连续性,无法在输出端获取另一种偏振态,如图6(b)所示。因此,如何同时获取分离后的两种偏振态仍然是一个难题。

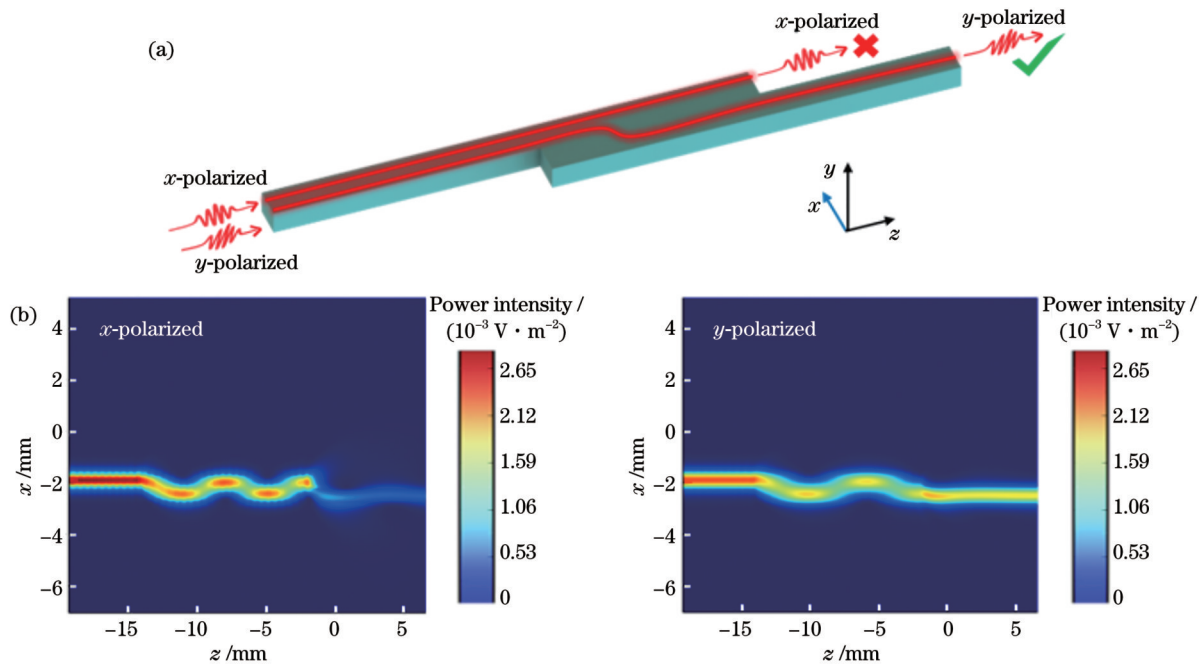


图6 定向耦合器结构示意图以及两种正交偏振模式在其中的功率分布。(a)沿x轴放置的定向耦合器示意图(箭头曲线表示定向耦合器中x偏振态和y偏振态的传输路径,x轴表示亚波长光纤的放置方向);(b)工作频率为0.25 THz时x偏振态和y偏振态在定向耦合器中的功率分布

Fig. 6 Schematic of directional coupler and power distributions of two orthogonal polarization modes. (a) Schematic of directional coupler placed along x -axis (arrow lines indicate propagation paths of both x -polarized and y -polarized states for directional coupler, x -axis represents placement direction for subwavelength fibers); (b) simulated power distributions of directional coupler for x -polarized and y -polarized states at 0.25 THz

得益于上述弯曲光纤的低弯曲损耗,首先设计了引入弯曲半径为10 mm的90°弯曲光纤的定向耦合器,以同时获取两种正交偏振模式。为了提高定向耦合器的耦合性能,将两个直光纤紧贴在一起。在此基础上,与弯曲光纤进行级联,根据光纤的两种弯曲方向和两种放置方向进行组合,设计了图7所示的4种定向耦合器。图7中箭头曲线表示定向耦合器中x偏振态和y偏振态的传输路径。图7(a)、(b)中x轴及图7(c)、(d)中y轴表示光纤的弯曲方向;图7(a)、(c)中x轴及图7(b)、(d)中y轴表示亚波长光纤的放置方向。

值得注意的是,传统的耦合模理论不再适用于引入亚波长弯曲光纤的定向耦合器,模式耦合不仅发生在相邻的两根直光纤上,也发生在弯曲光纤与直光纤之间的区域。因此,需要对每种定向耦合器的耦合长度进行手动调整,使其在工作频率处具备

最佳的耦合性能。为了评估耦合器的性能,引入了ER的概念,其中x偏振态和y偏振态的ER^[35-36]分别表示为

$$R_E^{(x)} = 10 \lg \frac{P_{\text{out}}^{(x)}}{P_{\text{out}}^{(y)}}, \quad (1)$$

$$R_E^{(y)} = 10 \lg \frac{P_{\text{out}}^{(y)}}{P_{\text{out}}^{(x)}}, \quad (2)$$

式中: $P_{\text{out}}^{(x)}$ 和 $P_{\text{out}}^{(y)}$ 分别为太赫兹波在输出端口的输出功率。对工作频率为0.25 THz时定向耦合器的传输率和ER进行了分析,x偏振态和y偏振态的传输率和ER曲线随耦合长度的变化呈准周期性变化,如图8所示。从图8中可以看出,当耦合长度为特定值时,定向耦合器的整体性能最佳,其中每个耦合器所选的耦合长度在图中用虚线标出。将定向耦合器的耦合长度设为选定值,从而实现对引入弯曲光纤的定向耦合器的优化。

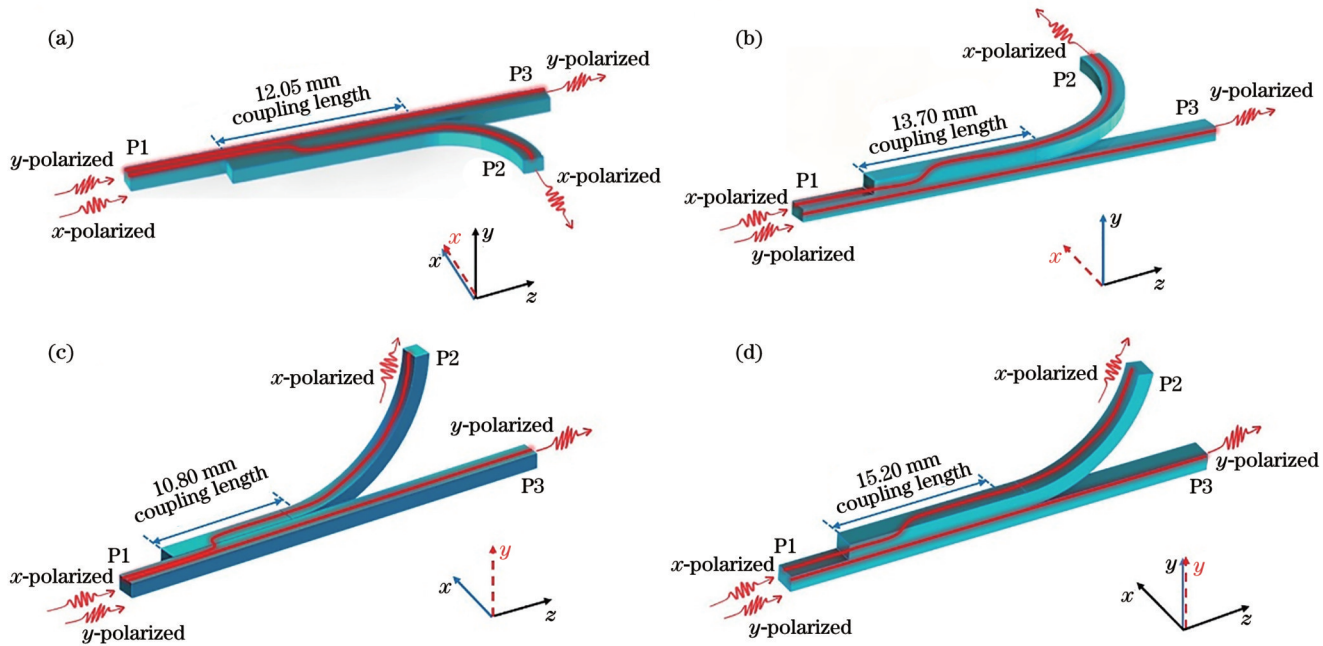


图 7 4 种定向耦合器的结构示意图。(a) 沿 x 轴放置 x 轴弯曲的定向耦合器;(b) 沿 y 轴放置 x 轴弯曲的定向耦合器;(c) 沿 x 轴放置 y 轴弯曲的定向耦合器;(d) 沿 y 轴放置 y 轴弯曲的定向耦合器

Fig. 7 Schematics of four types of directional couplers. (a) x -placed x -bent directional coupler; (b) y -placed x -bent directional coupler; (c) x -placed y -bent directional coupler; (d) y -placed y -bent directional coupler

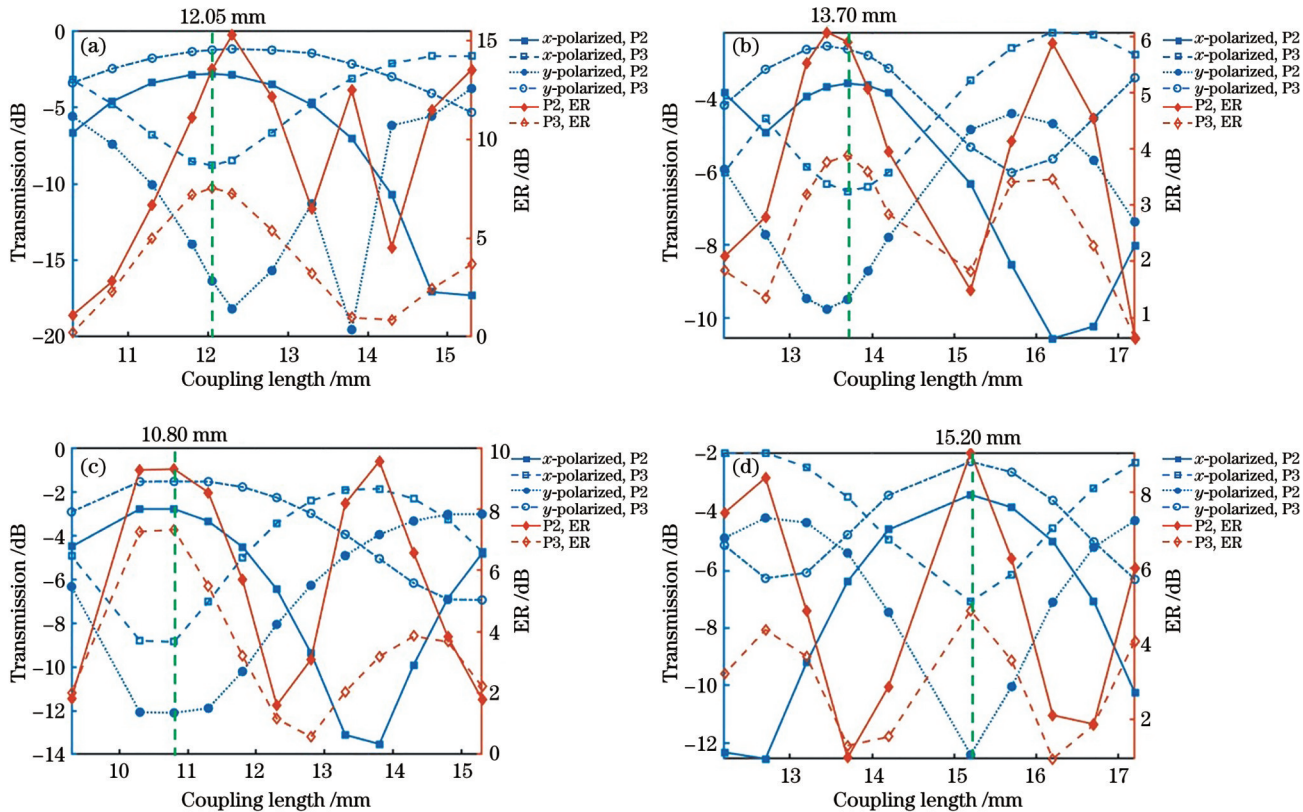


图 8 4 种定向耦合器在 0.25 THz 工作频率处的传输率和 ER 随耦合长度的变化曲线。(a) 沿 x 轴放置 x 轴弯曲的定向耦合器;(b) 沿 y 轴放置 x 轴弯曲的定向耦合器;(c) 沿 x 轴放置 y 轴弯曲的定向耦合器;(d) 沿 y 轴放置 y 轴弯曲的定向耦合器

Fig. 8 Transmissions and ER values for four directional couplers as functions of coupling length at operating frequency of 0.25 THz. (a) x -placed x -bent directional coupler; (b) y -placed x -bent directional coupler; (c) x -placed y -bent directional coupler; (d) y -placed y -bent directional coupler

调整完4种定向耦合器的耦合长度后,还需要分析0.24~0.28 THz工作频率范围内的频率响应。

图9为4种定向耦合器的传输率随频率的变化和ER随频率的变化。从图9中可以看出,在0.24~0.28 THz的宽带范围内,沿x轴放置x轴弯曲的定向耦合器有着最高的传输率和ER。在目标频率为0.25 THz时,x偏振态和y偏振态的传输率分别为-2.82 dB和-1.26 dB,而ER分别高达13.54 dB和7.54 dB。此

外,考虑到实际应用,分析了沿x轴放置的x轴弯曲定向耦合器的耦合长度容差。对于该耦合器,当耦合长度在11.8~12.3 mm范围内(容差为0.5 mm)时,x偏振态和y偏振态都能获得高传输率(高于-3 dB)和高ER(高于7 dB)。图10分别展示了x偏振态和y偏振态在定向耦合器中xz平面上的功率分布,以证明该耦合器对两种正交偏振模式的分离能力。

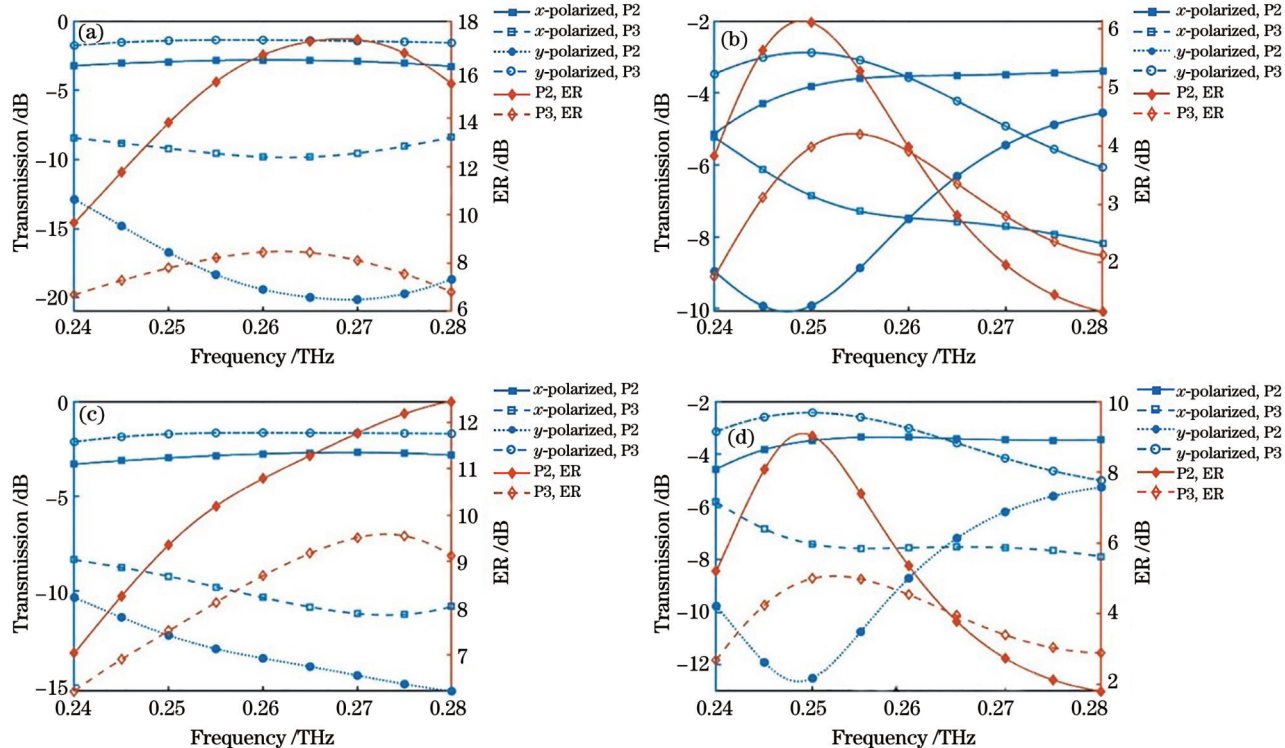


图9 4种定向耦合器的传输率和ER随频率的变化。(a)沿x轴放置x轴弯曲的定向耦合器;(b)沿y轴放置x轴弯曲的定向耦合器;(c)沿x轴放置y轴弯曲的定向耦合器;(d)沿y轴放置y轴弯曲的定向耦合器

Fig. 9 Transmission and ER values for four directional couplers as functions of frequency. (a) x -placed x -bent directional coupler; (b) y -placed x -bent directional coupler; (c) x -placed y -bent directional coupler; (d) y -placed y -bent directional coupler

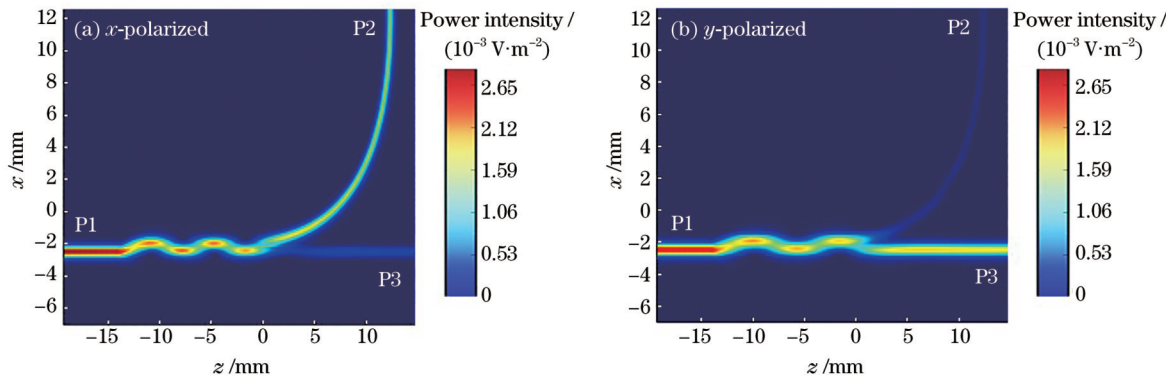


图10 0.25 THz频率处x偏振态和y偏振态在沿x轴放置的x轴弯曲定向耦合器中xz平面上的功率分布。(a)x偏振态;(b)y偏振态

Fig. 10 Power distributions on xz -plane of x -polarized and y -polarized states at 0.25 THz for x -placed x -bent directional coupler. (a) x -polarized state; (b) y -polarized state

接下来对引入S型弯曲光纤的定向耦合器进行设计。沿x轴放置x轴弯曲和沿x轴放置y轴弯曲定向

耦合器的结构如图11(a)、(b)所示。图11中箭头曲线表示定向耦合器中x偏振态和y偏振态的传输路径;

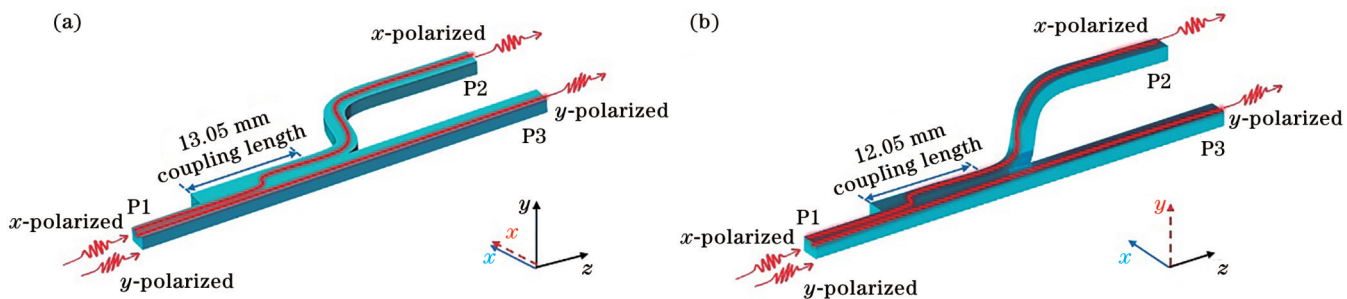


图11 引入S型弯曲光纤的定向耦合器结构图。(a)沿x轴放置x轴弯曲定向耦合器;(b)沿x轴放置y轴弯曲定向耦合器
Fig. 11 Schematics of directional couplers consisting of S-shaped bending fibers. (a) x -placed x -bent directional coupler; (b) x -placed y -bent directional coupler

图11(a)中 x 轴及图11(b)中 y 轴表示光纤的弯曲方向;图11(a)、(b)中 x 轴表示亚波长光纤的放置方向。本文只介绍了沿 x 轴放置的耦合器,而沿 y 轴放置的耦合器可采用与引入90°弯曲光纤的耦合器类似的方法进行设计。这两种定向耦合器的耦合性能如图12所示,在0.27 THz时都具有较高的传输率和ER,可用于器件集成。如图1(a)所示,本文选用沿 x 轴放置 y

轴弯曲的定向耦合器用于频率复用。此外,频率为0.27 THz的 x 偏振态和 y 偏振态在该耦合器中的功率分布如图13所示,为直观显示,将沿 y 轴弯曲的S型光纤的功率分布从 yz 平面转移到了 xz 平面上。不同于在2D平面上集成的平面器件,本文提出的光纤器件在3D空间内都可以进行集成,输入和输出端口可以设计在任意空间位置,这极大提高了器件应用的灵活性。

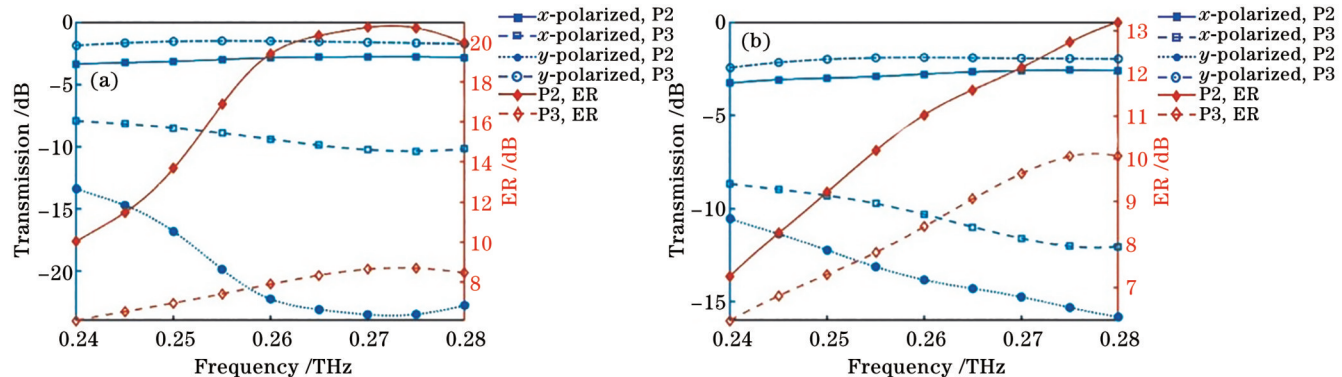


图12 两种定向耦合器的传输率和ER随频率的变化曲线。(a)沿x轴放置x轴弯曲的定向耦合器;(b)沿x轴放置y轴弯曲的定向耦合器
Fig. 12 Transmission and ER values of two directional couplers as functions of frequency. (a) x -placed x -bent directional coupler; (b) x -placed y -bent directional coupler

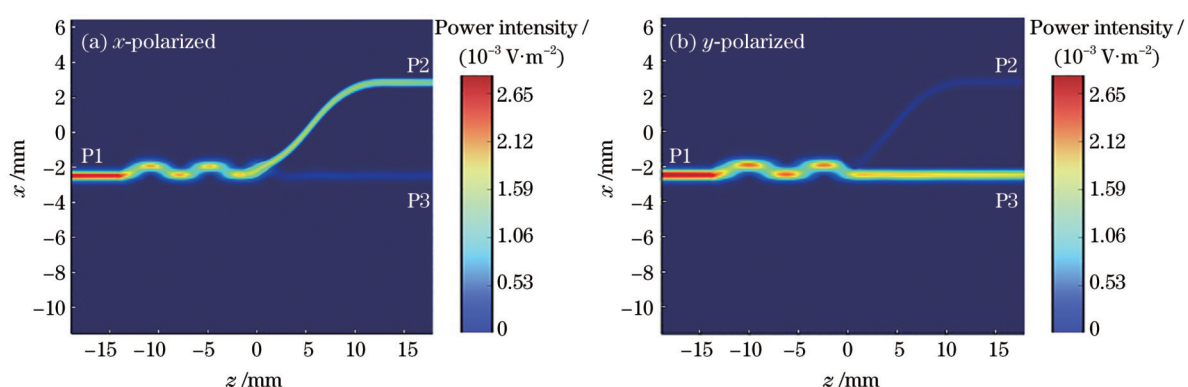


图13 在0.27 THz频率处沿x轴放置y轴弯曲定向耦合器中的功率分布。(a)x偏振态;(b)y偏振态
Fig. 13 Simulated power distributions at 0.27 THz for x -placed y -bent directional coupler. (a) x -polarized state; (b) y -polarized state

3.3 光纤光栅

太赫兹光纤布拉格光栅在构建信号处理和环境

传感器件方面起着极为关键的作用。太赫兹光纤通道通常会在有线传输链路上引入信号色散(典型值

为 $4 \text{ ps} \cdot \text{THz}^{-1} \cdot \text{mm}^{-1}$ ^[30],为了补偿传输色散,本课题组利用微机械加工技术制作了均匀光栅^[28]。本文以0.25 THz为目标频率,重新对均匀布拉格光栅进行设计,其仿真参数分别为: $d_{1x}=0.600 \text{ mm}$, $d_{1y}=0.445 \text{ mm}$, $d_{2x}=0.320 \text{ mm}$, $d_{2y}=0.237 \text{ mm}$, $N=30$, $\Lambda=0.588 \text{ mm}$, $L_1/\Lambda=0.6$,如图14(a)、(b)

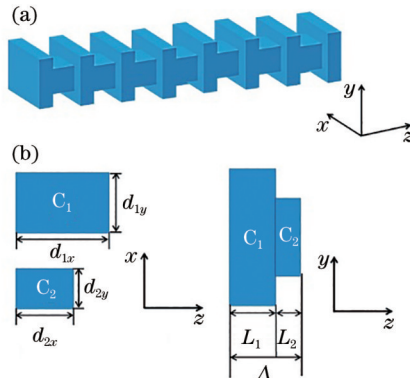


图14 色散补偿器的结构和仿真结果。(a)色散补偿器的整体结构;(b)光栅单元在xz平面和yz平面上的截面参数;(c)色散补偿器的传输率和群速度色散随频率变化的曲线

Fig. 14 Structure and simulation results of dispersion compensator. (a) Schematic of dispersion compensator; (b) single grating unit cross-sections in xz -plane and yz -plane; (c) transmission and GVD values of dispersion compensator as functions of frequency

基于本课题组的前期工作^[10],本文设计了一种基于光纤相移光栅的传感器,用于对环境RI变化进行监测。值得注意的是,为了监测周围环境的RI变化, π 相移光栅不能封装在泡沫包层内。如图15(a)、(b)所示,该相移光栅的仿真参数分别

所示,其中, N 为光栅的周期数, Λ 为单个光栅周期的长度, C_1 代表大尺寸光栅单元, C_2 代表小尺寸光栅单元。如图14(c)所示,该均匀光栅以额外引入3.17 dB的插入损耗为代价,为0.25 THz的x偏振态提供 $-109.4 \text{ ps} \cdot \text{THz}^{-1} \cdot \text{mm}^{-1}$ 的色散补偿量。

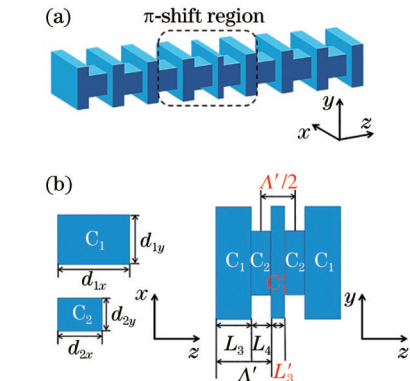
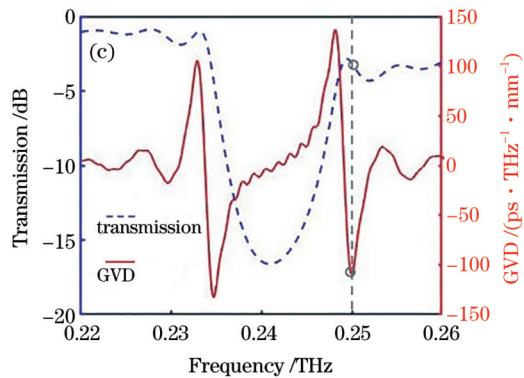


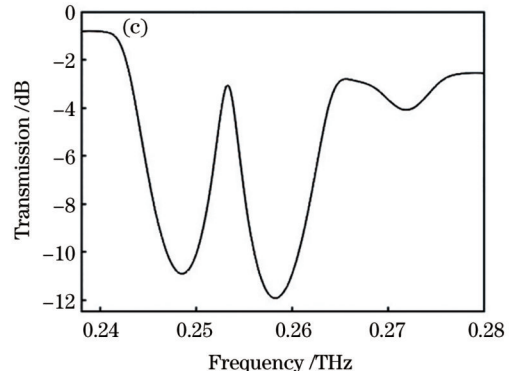
图15 相移光栅的结构和仿真结果。(a)相移光栅的整体结构;(b)光栅单元在xz平面和yz平面上的截面参数;(c)相移光栅中y偏振态的传输率随频率变化的曲线

Fig. 15 Structure and simulation results of π -shifted grating. (a) Schematic of π -shifted grating; (b) single grating unit cross-sections in xz -plane and yz -plane; (c) transmission for y -polarized state of π -shifted grating as a function of frequency

3.4 多维复用与RI传感集成器件

本文研究了由矩形亚波长光纤、弯曲光纤、50/50 Y型分束器、定向耦合器、均匀光栅以及相移光栅组成的太赫兹多维复用与RI传感集成器件[图1(a)]。图16中白色区域表示归一化模式功率低于1%的包层区域,为了方便显示,将沿x轴放置的y轴弯曲定向耦合器的功率分布从yz平面转移到了xz平面。不同

为: $N=29$, $\Lambda'=0.544 \text{ mm}$, $L'_3=0.056 \text{ mm}$, $L_3/\Lambda'=0.8$ 。图15中, C'_1 代表改变长度后的大尺寸光栅单元, Λ' 代表单个光栅周期的长度。如图15(c)所示, π 相移光栅传输峰的FWHM和ER分别为2.6 GHz和8.86 dB。



偏振态和频率的太赫兹信号可通过该器件进行复用和解复用。该器件首先进行偏振解复用操作,0.25 THz的x偏振态通过第一个定向耦合器与0.25 THz的y偏振态分离,然后利用均匀光栅进行色散补偿。如图17(a)所示,下行端口输出的0.25 THz的x偏振态的传输率和ER分别为 -5.94 dB 和 15.16 dB 。以基于亚波长光纤的1.3 m有线通信链路为例[如图2(d)

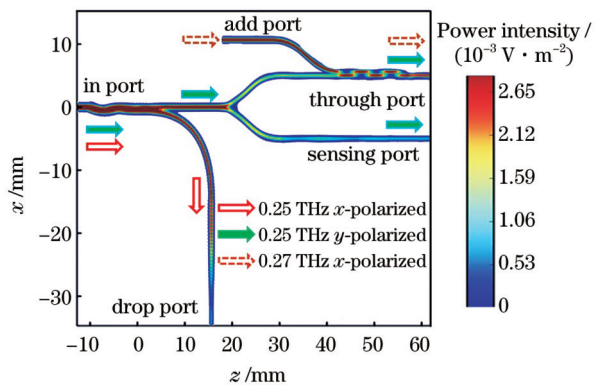
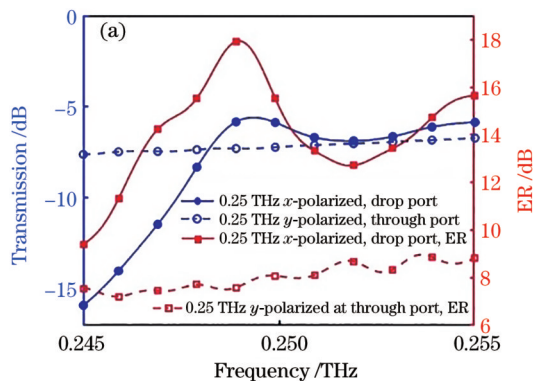


图16 不同偏振和不同频率的信号在多维复用与传感集成器件中的功率分布

Fig. 16 Simulated power distribution for modes propagating along multidimensional-multiplexing and sensing integrated device



所示,0.25 THz的x偏振态在光纤中的群速度色散为 $1.48 \text{ ps} \cdot \text{THz}^{-1} \cdot \text{mm}^{-1}$,完全补偿链路中引入的群速度色散所需的光栅长度约为17.6 mm。然后,从添加端口发射0.27 THz的x偏振信号,该信号与通过Y型分束器上支路传输的0.25 THz的y偏振信号进行频率复用。如图17(a)、(b)所示,通过直通端口的0.25 THz的y偏振态的传输率为-7.20 dB,ER为8.06 dB,而0.27 THz的x偏振态的传输率为-2.02 dB。在环境RI传感方面,由于环境RI与传输峰的中心频率呈线性关系,通过与Y型分束器的下支路级联的 π 相移光栅输出的传输峰的中心频率可以得出周围环境的RI。如图18所示,当RI从1.00增加到1.02时,传输峰的中心频率发生红移,传感器的灵敏度为0.181 THz/RIU。图18(a)中箭头表示随着周围RI的增加,传输峰的中心频率发生红移。

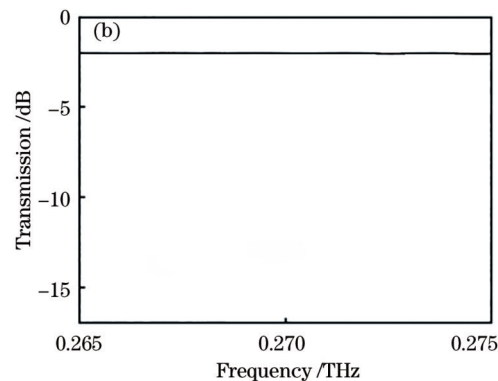


图17 不同偏振信号的传输率和ER随频率的变化曲线。(a)中心频率为0.25 THz的x偏振态和y偏振态窄带信号在集成器件的下行端口和直通端口的传输率和ER随频率的变化曲线;(b)中心频率为0.27 THz的x偏振态窄带信号在集成器件直通端口的传输率随频率的变化曲线

Fig. 17 Transmission and ER values for signals with different polarizations as functions of frequency. (a) Transmission and ER values of x-polarized and y-polarized narrowband signals with a central frequency of 0.25 THz at drop port and through port for integrated device as functions of frequency; (b) transmission of x-polarized narrowband signal with central frequency of 0.27 THz at through port for integrated device as a function of frequency

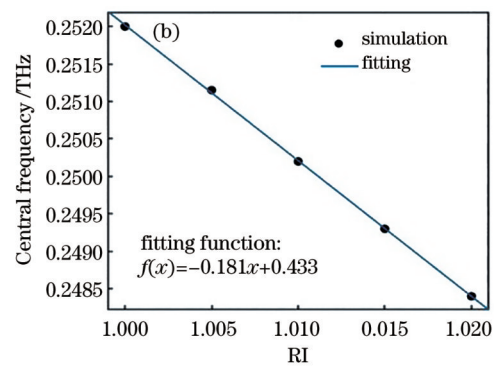
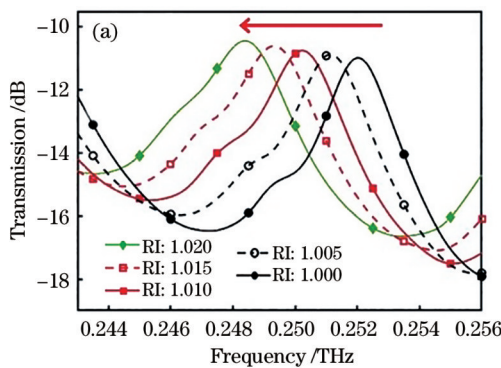


图18 不同环境RI下相移光栅的传输谱以及中心频率随RI的变化。(a)相移光栅的传输谱;(b)传输谱中心频率随RI的变化曲线

Fig. 18 Transmission spectra of phase-shifted grating under different refractive indices and center frequency varying with RI.

(a) Transmission spectra of phase-shifted grating; (b) central frequency of transmission spectrum as a function of RI

4 结论

本文提出了一种基于太赫兹波长双折射光纤的

多维复用与RI传感集成器件。首先,通过引入弯曲光纤设计了高传输率和高ER的定向耦合器,实现了偏振和频率(解)复用功能。其次,利用集成器件中的均

匀光栅和相移光栅分别实现了色散补偿和环境 RI 感知。太赫兹亚波长光纤器件具有 3D 空间集成、高效传输等方面的优势,为太赫兹波传输-操控-感知一体化信息系统提供了新颖的设计方案。此外,太赫兹光纤平台有望进一步集成信号调制、高分辨率成像等有源、无源功能器件,为太赫兹信息系统落地提供技术支撑。

参 考 文 献

- [1] Xu G F, Skorobogatiy M. Wired THz communications[J]. *Journal of Infrared, Millimeter, and Terahertz Waves*, 2022, 43(9): 728-778.
- [2] Dang S P, Amin O, Shihada B, et al. What should 6G be?[J]. *Nature Electronics*, 2020, 3: 20-29.
- [3] Nagatsuma T, Ducournau G, Renaud C C. Advances in terahertz communications accelerated by photonics[J]. *Nature Photonics*, 2016, 10: 371-379.
- [4] Kumar A, Gupta M, Singh R. Topological integrated circuits for 5G and 6G[J]. *Nature Electronics*, 2022, 5: 261-262.
- [5] 李丽, 葛宏义, 蒋玉英, 等. 太赫兹波在6G通信网络中的研究进展[J]. 激光与光电子学进展, 2022, 59(13): 1300007.
- [6] 蔡杰, 耿易星, 余金清, 等. 强激光太赫兹辐射源研究现状与发展趋势分析[J]. 中国激光, 2023, 50(17): 1714009.
- Cai J, Geng Y X, Yu J Q, et al. Analysis of current status and development trends of terahertz radiation sources based on strong laser pulses[J]. *Chinese Journal of Lasers*, 2023, 50(17): 1714009.
- [7] 钟粤华, 韩玉柱, 赖志鸿, 等. 拓扑半金属二碲化铂太赫兹探测器[J]. 光学学报, 2022, 42(15): 1504001.
- Zhong Y H, Han Y Z, Lai Z H, et al. Topological semimetal PtTe₂ terahertz detector[J]. *Acta Optica Sinica*, 2022, 42(15): 1504001.
- [8] Sen P, Siles J V, Thawdar N, et al. Multi-kilometre and multi-gigabit-per-second sub-terahertz communications for wireless backhaul applications[J]. *Nature Electronics*, 2023, 6: 164-175.
- [9] Kumar A, Gupta M, Pitchappa P, et al. Phototunable chip-scale topological photonics: 160 Gbps waveguide and demultiplexer for THz 6G communication[J]. *Nature Communications*, 2022, 13(1): 5404.
- [10] Li H S, Atakaramians S, Yuan J, et al. Terahertz polarization-maintaining subwavelength filters[J]. *Optics Express*, 2018, 26(20): 25617-25629.
- [11] Cao Y, Nallappan K, Guerboukha H, et al. Additive manufacturing of highly reconfigurable plasmonic circuits for terahertz communications[J]. *Optica*, 2020, 7(9): 1112-1125.
- [12] Liu F, Cui Y H, Masouros C, et al. Integrated sensing and communications: toward dual-functional wireless networks for 6G and beyond[J]. *IEEE Journal on Selected Areas in Communications*, 2022, 40(6): 1728-1767.
- [13] Kumar A, Gupta M, Pitchappa P, et al. Terahertz topological photonic integrated circuits for 6G and beyond: a perspective[J]. *Journal of Applied Physics*, 2022, 132(14): 140901.
- [14] Ong J R, Ang T Y L, Sahin E, et al. Broadband silicon polarization beam splitter with a high extinction ratio using a triple-bent-waveguide directional coupler[J]. *Optics Letters*, 2017, 42(21): 4450-4453.
- [15] Shen B, Wang P, Polson R, et al. An integrated-nanophotonics polarization beamsplitter with $2.4 \times 2.4 \mu\text{m}^2$ footprint[J]. *Nature Photonics*, 2015, 9: 378-382.
- [16] 朱国锋, 戴圳榕, 居学尉, 等. 基于逆向设计的片上太赫兹解复用器和光栅耦合器[J]. 光学学报, 2022, 42(9): 0913001.
- Zhu G F, Dai Z R, Ju X W, et al. On-chip terahertz demultiplexer and grating coupler based on reverse design[J]. *Acta Optica Sinica*, 2022, 42(9): 0913001.
- [17] Deng W T, Chen L, Zhang H Q, et al. On-chip polarization-and frequency-division demultiplexing for multidimensional terahertz communication[J]. *Laser & Photonics Reviews*, 2022, 16(10): 2200136.
- [18] Atakaramians S, Afshar V S, Monro T M, et al. Terahertz dielectric waveguides[J]. *Advances in Optics and Photonics*, 2013, 5(2): 169-215.
- [19] Lu J T, Lai C H, Tseng T F, et al. Terahertz pipe-waveguide-based directional couplers[J]. *Optics Express*, 2011, 19(27): 26883-26890.
- [20] Wang Z, Dai Z J, Chen M Y, et al. Terahertz beam splitter based on mode coupling of subwavelength waveguides[J]. *Optics Communications*, 2022, 517: 128294.
- [21] Weidenbach M, Jahn D, Rehn A, et al. 3D printed dielectric rectangular waveguides, splitters and couplers for 120 GHz[J]. *Optics Express*, 2016, 24(25): 28968-28976.
- [22] Ma T, Nallapan K, Guerboukha H, et al. Analog signal processing in the terahertz communication links using waveguide Bragg gratings: example of dispersion compensation[J]. *Optics Express*, 2017, 25(10): 11009-11026.
- [23] Liu Y J, Khan M T A, Atakaramians S, et al. Terahertz polarization-maintaining sampled gratings for dual-frequency filtering and dispersion compensation[J]. *Results in Physics*, 2022, 39: 105721.
- [24] Cao Y, Nallappan K, Xu G F, et al. Add drop multiplexers for terahertz communications using two-wire waveguide-based plasmonic circuits[J]. *Nature Communications*, 2022, 13(1): 4090.
- [25] Yuan J, Li Z R, Ning T G, et al. Subwavelength waveguide-based THz narrow bandpass filter and application in refractive-index sensing[J]. *Results in Physics*, 2020, 19: 103299.
- [26] Islam M S, Cordeiro C M B, Franco M A R, et al. Terahertz optical fibers[J]. *Optics Express*, 2020, 28(11): 16089-16117.
- [27] Islam M S, Cordeiro C M B, Nine M J, et al. Experimental study on glass and polymers: determining the optimal material for potential use in terahertz technology[J]. *IEEE Access*, 2020, 8: 97204-97214.
- [28] Khan M T A, Li H S, Liu Y J, et al. Compact terahertz birefringent gratings for dispersion compensation[J]. *Optics Express*, 2022, 30(6): 8794-8803.
- [29] Siddique N, Li Y G, Li H S, et al. Design of 130–290 GHz rectangular COC fibers for high-speed data links[C]//2021 51st European Microwave Conference (EuMC), April 4–6, 2022, London, United Kingdom. New York: IEEE Press, 2022: 397-400.
- [30] Nallappan K, Cao Y, Xu G F, et al. Dispersion-limited versus power-limited terahertz communication links using solid core subwavelength dielectric fibers[J]. *Photonics Research*, 2020, 8(11): 1757.
- [31] COMSOL. COMSOL 多物理场仿真软件[CP/OL]. (2023-10-18)[2023-10-23]. <https://cn.comsol.com/>.
- COMSOL. Multi physics field simulation software[CP/OL]. (2023-10-18)[2023-10-23]. <https://cn.comsol.com/>.
- [32] Deng W T, Chen L, Yuan S X, et al. Silicon-based integrated terahertz polarization beam splitters[J]. *Journal of Lightwave Technology*, 2022, 40(1): 170-178.
- [33] Chen H Z, Yan G F, Forsberg E, et al. Terahertz polarization splitters based on total and partial coupling in dual slotted core polymer fiber: comparison and analysis[J]. *IEEE Photonics Journal*, 2017, 9(3): 7103315.
- [34] 黄旭, 骆兴芳, 左翔宇, 等. 双芯太赫兹光纤定向耦合器[J]. 光学学报, 2022, 42(2): 0206006.
- Huang X, Luo X F, Zuo X Y, et al. Dual-core terahertz fiber

- directional coupler[J]. *Acta Optica Sinica*, 2022, 42(2): 0206006.
- [35] Zhang X S, Liu Z J, Gui Y M, et al. Characteristics and preparation of a polarization beam splitter based on a chalcogenide dual-core photonic crystal fiber[J]. *Optics Express*, 2021, 29(24): 39601-39610.
- [36] Chen Y F, Zhang J, Zhu M, et al. Ultra-compact and broadband all-silicon TM-pass power splitter using subwavelength holey-structured metamaterial waveguides[J]. *Optics Express*, 2022, 30(25): 44604-44616.

Terahertz Multidimensional-Multiplexing and Refractive-Index-Sensing Integrated Device

Jie Lu, Li Haisu*, Liu Yajing, Wang Jianshuai, Ren Guobin, Pei Li

*Key Laboratory of All Optical Network and Advanced Telecommunication Network, Ministry of Education,
Institute of Lightwave Technology, Beijing Jiaotong University, Beijing 100044, China*

Abstract

Objective Terahertz waves featuring broad bandwidths play an increasingly important role in next-generation communication systems. For both terahertz wired and wireless communications, terahertz waveguide integrated devices providing “on-line” signal processing functionalities are in vital demand. In the next-generation communication system, the multiplexing technology around the electromagnetic wave physical parameters such as terahertz radiation polarization, frequency, and phase is an effective solution to enhancing spectrum efficiency. Additionally, the future Internet of Everything information system should have a real-time monitoring function of communication environmental parameters (temperature, humidity, etc.). Given the above technical requirements of multidimensional multiplexing and environmental sensing, novel terahertz functional integrated devices for high-speed information transmission-manipulation-perception fusion should be studied urgently. Several terahertz silicon-based waveguide devices have been demonstrated, but the planar structure restricts the spatial degree of freedom for the devices, which means the devices can only be integrated in a 2D plane. Terahertz fiber-based devices are substrate-free to provide terahertz wave routing abilities along any spatial direction. Nevertheless, most of the reported terahertz fiber devices offer a single functionality, remaining a significant scope of multiple device integration. Thus, we propose a polarization-maintaining subwavelength fiber-based multidimensional multiplexing and sensing integrated device which is composed of fiber bends, a 50/50 Y-splitter, directional couplers, and Bragg gratings. The proposed fiber device provides (de)multiplexing in an additional direction that is orthogonal to the 2D space in contrast to the planar devices. Meanwhile, the device integrates multiple functionalities, including frequency- and polarization-(de)multiplexing, dispersion compensation, and surrounding refractive index sensing. In a nutshell, the integrated device provides exciting perspectives for boosting transmission capacity and developing communication-sensing integration of the next-generation communication systems.

Methods The finite element analysis method and finite-difference time-domain model are employed in our study. First, the finite element analysis method is adopted to calculate the transmission parameters (fractional power in the core, loss, group velocity dispersion, etc.) of terahertz subwavelength fibers with different cross-sectional parameters to design polarization-maintaining fibers supporting low-loss and low-dispersion transmission. Then, S-shaped and 90° bending fibers are designed using Bessel curves. Furthermore, the finite-difference time-domain model is utilized to analyze the transmission characteristics of S-shaped and 90° bending fibers. Then, two S-shaped bending fibers with the same bending radius are utilized to form a Y-splitter. In the next step, we leverage the supermode theory as a theoretical guide and the finite element analysis method as a tool to calculate the required coupling length of the directional couplers. Additionally, the finite element analysis method is employed to investigate the effects of grating cell cross-section parameters, thickness, and number of cycles on grating performance (e.g., transmission and dispersion compensation), and thus accomplish the structural design of uniform gratings. Finally, the performance of the proposed terahertz devices including directional couplers, Y-splitter, uniform grating, and phase-shifted grating is simulated and analyzed using the time-domain finite difference method.

Results and Discussions We present terahertz subwavelength rectangular fibers, bending fibers, Y-splitter, directional couplers, uniform grating, phase-shift grating, and multidimensional-multiplexing and refractive-index-sensing integrated devices. First, the subwavelength fiber supports low-loss (below 0.051 dB/mm) and high-birefringent (beyond 0.03)

transmissions at a target bandwidth over 0.24–0.28 THz as shown in Fig. 2. Second, the transmission of S-shaped bending fibers with a bending radius of 10 mm is slightly higher than that of 90° bending fibers in the frequency range of 0.24–0.28 THz, whose transmission is higher than -1 dB at the operating frequency of 0.25 THz [Fig. 4(d)]. Thanks to the high transmission of x -bent S-shaped bends, a 50/50 Y-splitter can be readily designed using two bends with the same radius of 10 mm. Third, for the x -placed x -bent directional coupler, high transmission (above -3 dB) and high ER (above 7 dB) are obtained for both x -polarization and y -polarization modes when coupling lengths are in the range of 11.8–12.3 mm. Finally, the integrated device achieves simultaneously polarization and frequency (de)multiplexing, with high transmissions [drop port: -5.94 dB for 0.25 THz x -polarization with dispersion compensation; through port: -7.20 dB for 0.25 THz y -polarization, -2.02 dB for 0.27 THz x -polarization] and high ER (drop port: 15.16 dB; through port: 8.06 dB). Additionally, the device integrates fiber Bragg gratings, allowing both zero-GVD dispersion compensation and refractive-index sensing (sensitivity of 0.181 THz/RIU) abilities (Figs. 17 and 18).

Conclusions We propose and analyze a terahertz multidimensional-multiplexing and sensing integrated device based on subwavelength birefringent fibers, composed of fiber bends, 50/50 Y-splitter, directional couplers, and Bragg gratings. First, a directional coupler with high transmission and high extinction ratio is designed by introducing a bent fiber to achieve polarization and frequency (de)multiplexing functions. Second, the uniform grating and phase-shift grating in the integrated device enable dispersion compensation and environmental refractive index sensing respectively. Terahertz subwavelength fiber devices feature dense integration in 3D space and efficient transmission, which provides novel design solutions for the integrated terahertz wave transmission-manipulation-sensing information system. Meanwhile, we also envision that many more components such as modulators and imaging devices will be further integrated on the terahertz fiber platform.

Key words optical device; terahertz; coupler; multiplexer; sensor